Int. J. Heat Mass Transfer. Vol. 36, No. 8, pp. 2069–2082, 1993
Printed in Great Britain

0017-9310/93 $6.00+0.00

Periodically developed flow and heat transfer in a ribbed duct

S. ACHARYA, S. DUTTA, T. A. MYRUM and R. S. BAKER
Mechanical Engineering Department, Louisiana State University, Baton Rouge, LA 70803, U.S.A.

(*Received* 18 *June* 1992 *and in final form* 19 *October* 1992)

Abstract—Periodic fully developed flow and heat transfer results for a ribbed duct were obtained experimentally and numerically, using the nonlinear and standard k–ε turbulence models. Predicted recirculation lengths and maximum Nusselt number locations agreed well with the measured values. Both models performed poorly in the separated region just behind the ribs, where the Reynolds stresses were grossly underpredicted, the flow temperatures were overpredicted, and the mean velocity magnitudes were generally underpredicted. The local Nusselt numbers were underpredicted by both models. The nonlinear model predicted more realistic Reynolds stresses in the core flow region immediately above the ribs than the standard k–ε model.

INTRODUCTION

THE PERIODIC deployment of roughness elements (ribs) along the length of rectangular, circular, and annular ducts is a well-established heat transfer augmentation technique with numerous applications. Sparrow and Tao [1] found that the presence of periodic, two-dimensional ribs in a rectangular duct results in the rapid establishment of a periodic fully developed regime. Patankar *et al.* [2] were able to solve for the periodic fully developed laminar flow and heat transfer over a periodic module, without involving the entrance length problem. Lee *et al.* [3] used the generalized method of ref. [2] and the standard k–ε turbulence model with and without the curvature correction developed by Leschziner and Rodi [4] to solve for the turbulent flow field and heat transfer between successive ribs in the periodic fully developed regime of a ribbed annulus. Comparisons between the calculated results and experimental results were limited to a single streamwise velocity profile at about midway between the successive ribs in the region above the plane of the upper surface of the ribs, a single temperature distribution at about midway between the ribs, mean pressure gradients, and average Nusselt numbers. On the whole, the standard k–ε model with curvature correction performed better than the standard k–ε model without curvature correction.

The chief objective of the present work is to examine the ability of the nonlinear k–ε turbulence model [5] to predict the flow and heat transfer between successive two-dimensional ribs in the periodic fully developed region of an asymmetrically heated, rectangular duct with ribs periodically distributed along the uniformly heated bottom wall. This objective will be accomplished by comparing the nonlinear model results to the results obtained using the standard k–ε model [6] and to the results obtained in the experimental portion of this study, which consists of laser-Doppler flow measurements, flow temperature measurements, and local Nusselt number results deduced from local wall temperature measurements.

The decision to model the turbulent flow and heat transfer in the periodic fully developed regime using the nonlinear model was based on the fact that the nonlinear model includes the nonisotropic nature of the Reynolds stresses, a major source of error associated with using the standard k–ε model to predict separated flow behavior [7]. Speziale [5], Thangam and Speziale [7], Speziale and Ngo [8], Thangam and Hur [9], and Dutta [10] all obtained better predictions for separated flows past backsteps using the nonlinear model as opposed to using the standard k–ε model.

There are no studies in the open literature which report results obtained from applying the nonlinear model to the periodic fully developed regime of a ribbed duct. In fact, to the authors' knowledge, the aforementioned study of ref. [3] represents the only attempt to model the turbulent flow and heat transfer in the periodic fully developed regime of a ribbed duct, and the limited comparisons between the computed results and experimental results are the only published comparisons for this region.

Comparisons between k–ε model results, with and without curvature corrections, and experimental results have been made for flows past a single rib (see Durst and Rastogi [11], Benodekar *et al.* [12], Chung *et al.* [13], and Park and Chung [14]). The main thrust of these works was to examine the performance of various curvature correction techniques. It was found that curvature correction resulted in improved flow predictions.

More relevant to the present investigation are the studies involving turbulent flows past successive ribs. Laser-Doppler measurements and standard k–ε

NOMENCLATURE

C_1, C_2, C_μ turbulence model constants, $C_1 = 1.44$, $C_2 = 1.92$, $C_\mu = 0.09$
C_D nonlinear model constant, $C_D = 1.68$
G generation of kinetic energy
h, H rib height, channel height, $H = 9.6h$
k turbulent kinetic energy
Nu local Nusselt number
P production of kinetic energy, $\mu_t G$
p, p^* pressure, effective pressure
q, q'' total heat input, heat flux. $q = 85$ W, $q'' = 280$ W m^{-2}
T, T_b, T_W temperature, bulk temperature, wall temperature
u, u' streamwise velocity and its fluctuating component
$\overline{u'v'}$, $\overline{u_i'T'}$ turbulent stresses
u_{ref} mean velocity in the channel
v, v' cross-stream velocity and its fluctuating component
x_R reattachment length
y^+ dimensionless distance from wall.

Greek symbols
β mean pressure gradient
ε dissipation of kinetic energy
μ, μ_t, μ_{eff} viscosity, turbulent viscosity, effective viscosity, $\mu_{eff} = \mu + \mu_t$
σ_k, σ_ε turbulence Prandtl number for k and ε, $\sigma_k = 1.0$, $\sigma_\varepsilon = 1.3$.

model predictions of the mean and fluctuating streamwise velocities were obtained by Durst *et al.* [15] in a two-dimensional, fully developed turbulent channel flow in which two thin fences were mounted to the wall in succession. Liou *et al.* [16] obtained standard k–ε model predictions and laser-Doppler velocity measurements of the streamwise mean and fluctuating velocities in a developing channel flow where two two-dimensional rectangular ribs were attached to both the top and bottom walls in succession.

Other relevant studies of flows past successive ribs are the experimental studies of refs. [17–20]. These studies deduced Nusselt numbers from heat transfer measurements. Reference [18] confirmed the interrib peak to be at approximately 0.5 to 1.0 rib heights upstream of reattachment.

GOVERNING EQUATIONS

The standard k–ε model

The standard k–ε model [6] is based on the Boussinesq approximation:

$$-\overline{u_i'u_j'} = -\tfrac{2}{3}k\delta_{ij} + \frac{\mu_t}{\rho}\left(\frac{\partial u_i}{\partial x_j} + \frac{\partial u_j}{\partial x_i}\right). \quad (1)$$

It involves solving the modeled k and ε equations along with the continuity and momentum equations. Assuming two-dimensional, steady, constant-density flow, the modeled equation for the x-component of velocity is given by

$$\rho u\frac{\partial u}{\partial x} + \rho v\frac{\partial u}{\partial y} = -\frac{\partial p^*}{\partial x} + \frac{\partial}{\partial x}\left(\mu_{eff}\frac{\partial u}{\partial x}\right) + \frac{\partial}{\partial y}\left(\mu_{eff}\frac{\partial u}{\partial y}\right) + S_u. \quad (2)$$

A similar equation can be written for v. In the above equations

$$p^* = p + \tfrac{2}{3}\rho k; \quad \mu_{eff} = \mu + \mu_t; \quad \mu_t = C_\mu \rho\frac{k^2}{\varepsilon}. \quad (3)$$

The source terms for the x-momentum and the y-momentum equations are

$$S_u = \frac{\partial}{\partial x}\left(\mu_t\frac{\partial u}{\partial x}\right) + \frac{\partial}{\partial y}\left(\mu_t\frac{\partial v}{\partial x}\right);$$

$$S_v = \frac{\partial}{\partial x}\left(\mu_t\frac{\partial u}{\partial y}\right) + \frac{\partial}{\partial y}\left(\mu_t\frac{\partial v}{\partial y}\right). \quad (4)$$

The modeled transport equations for turbulent kinetic energy and dissipation, k and ε are expressed as

$$\rho u\frac{\partial k}{\partial x} + \rho v\frac{\partial k}{\partial y} = \frac{\partial}{\partial x}\left(\frac{\mu_t}{\sigma_k}\frac{\partial k}{\partial x}\right) + \frac{\partial}{\partial y}\left(\frac{\mu_t}{\sigma_k}\frac{\partial k}{\partial y}\right) + \mu_t G - \rho\varepsilon \quad (5)$$

$$\rho u\frac{\partial \varepsilon}{\partial x} + \rho v\frac{\partial \varepsilon}{\partial y} = \frac{\partial}{\partial x}\left(\frac{\mu_t}{\sigma_\varepsilon}\frac{\partial \varepsilon}{\partial x}\right) + \frac{\partial}{\partial y}\left(\frac{\mu_t}{\sigma_\varepsilon}\frac{\partial \varepsilon}{\partial y}\right) + C_1\mu_t G\frac{\varepsilon}{k} - C_2\rho\frac{\varepsilon^2}{k}. \quad (6)$$

For the temperature, the transport equation is again based on the Boussinesq approximation ($\overline{u_i'T'} = (\mu_t/\rho Pr_t)(\partial T/\partial x_i)$).

$$\rho u\frac{\partial T}{\partial x} + \rho v\frac{\partial T}{\partial y} = \frac{\partial}{\partial x}\left(\frac{\mu_t}{Pr_t}\frac{\partial T}{\partial x}\right) + \frac{\partial}{\partial y}\left(\frac{\mu_t}{Pr_t}\frac{\partial T}{\partial y}\right). \quad (7)$$

To account for the near-wall effects in the standard k–ε model, wall functions are used [6]. This requires the first interior grid point to be at a distance $y^+ > 11.5$ from the wall and requires modifying the diffusion coefficient at the wall to satisfy the law of the wall relationship.

The near-wall dissipation value is prescribed from

equilibrium as $\varepsilon = C_\mu^{3/4} k^{3/2}/y$, and the wall gradients of k and ε are set to zero.

The nonlinear k–ε model

The nonlinear k–ε model of ref. [5] retains the tensorially invariant eddy viscosity of the standard k–ε model and adds the second-order derivatives of the streamwise and cross-stream velocities to the Boussinesq approximation to account for the nonisotropic behavior in the turbulent stresses. These extra second-order terms are incorporated as the source terms in the momentum equations and in the k and ε transport equations. The source terms are kept frame indifferent and can be included in a standard computer program that solves Navier–Stokes type equations.

For two-dimensional separated flows, the individual components of the stress terms in the nonlinear model can be written as

$$-\rho\overline{u'^2} = -\tfrac{2}{3}\rho k + 2\rho C_\mu \frac{k^2}{\varepsilon}\frac{\partial u}{\partial x} + 4C_D \rho C_\mu^2 \frac{k^3}{\varepsilon^2}\left[-\frac{1}{3}\left(\frac{\partial u}{\partial x}\right)^2 - \frac{7}{12}\left(\frac{\partial u}{\partial y}\right)^2 - \frac{1}{6}\left(\frac{\partial u}{\partial y}\frac{\partial v}{\partial x}\right) + \frac{5}{12}\left(\frac{\partial v}{\partial x}\right)^2 + t_1\right] \quad (8)$$

$$-\rho\overline{v'^2} = -\tfrac{2}{3}\rho k + 2\rho C_\mu \frac{k^2}{\varepsilon}\frac{\partial v}{\partial y} + 4C_D \rho C_\mu^2 \frac{k^3}{\varepsilon^2}\left[-\frac{1}{3}\left(\frac{\partial v}{\partial y}\right)^2 - \frac{7}{12}\left(\frac{\partial v}{\partial x}\right)^2 - \frac{1}{6}\left(\frac{\partial u}{\partial y}\frac{\partial v}{\partial x}\right) + \frac{5}{12}\left(\frac{\partial u}{\partial y}\right)^2 + t_2\right] \quad (9)$$

$$-\rho\overline{u'v'} = \rho C_\mu \frac{k^2}{\varepsilon}\left(\frac{\partial u}{\partial y} + \frac{\partial v}{\partial x}\right) + 4C_D \rho C_\mu^2 \frac{k^3}{\varepsilon^2}\left[-\frac{\partial u}{\partial y}\frac{\partial v}{\partial y} - \frac{\partial u}{\partial x}\frac{\partial v}{\partial x} + t_3\right] \quad (10)$$

where

$$t_1 = \frac{\partial}{\partial x}\left(u\frac{\partial u}{\partial x}\right) + \frac{\partial}{\partial y}\left(v\frac{\partial u}{\partial x}\right);$$

$$t_2 = \frac{\partial}{\partial x}\left(u\frac{\partial v}{\partial y}\right) + \frac{\partial}{\partial y}\left(v\frac{\partial v}{\partial y}\right);$$

$$t_3 = \frac{\partial}{\partial x}\left(u\frac{1}{2}\left(\frac{\partial u}{\partial y} + \frac{\partial v}{\partial x}\right)\right) + \frac{\partial}{\partial y}\left(v\frac{1}{2}\left(\frac{\partial u}{\partial y} + \frac{\partial v}{\partial x}\right)\right). \quad (11)$$

If the above nonlinear approximations for the turbulent stresses are substituted into the momentum equations, the resulting equations will have the same form as in the standard k–ε model with the effective pressure defined as

$$p^* = p + \tfrac{2}{3}\rho k - 4C_D C_\mu \mu_t \frac{k}{\varepsilon}\left[-\frac{1}{3}\left(\frac{\partial u}{\partial x}\right)^2 + \frac{5}{12}\left(\frac{\partial u}{\partial y}\right)^2 + \frac{5}{12}\left(\frac{\partial v}{\partial x}\right)^2 - \frac{1}{6}\left(\frac{\partial u}{\partial y}\frac{\partial v}{\partial x}\right)\right]. \quad (12)$$

The source terms for the x-momentum and y-momentum equations in the nonlinear model can be expressed as

$$S_u = \frac{\partial}{\partial x}\left(\mu_t \frac{\partial u}{\partial x}\right) + \frac{\partial}{\partial y}\left(\mu_t \frac{\partial v}{\partial x}\right) + \frac{\partial}{\partial x} 4C_D C_\mu \mu_t \frac{k}{\varepsilon} \times \left[-\left(\frac{\partial u}{\partial y}\right)^2 + \frac{\partial}{\partial x}\left(u\frac{\partial u}{\partial x}\right) + \frac{\partial}{\partial y}\left(v\frac{\partial u}{\partial x}\right)\right] + \frac{\partial}{\partial y} 4C_D C_\mu \mu_t \frac{k}{\varepsilon}\left[\frac{\partial}{\partial x}\left(u\frac{1}{2}\left(\frac{\partial u}{\partial y} + \frac{\partial v}{\partial x}\right)\right) + \frac{\partial}{\partial y}\left(v\frac{1}{2}\left(\frac{\partial u}{\partial y} + \frac{\partial v}{\partial x}\right)\right) - \frac{\partial u}{\partial y}\frac{\partial v}{\partial y} - \frac{\partial u}{\partial x}\frac{\partial v}{\partial x}\right] \quad (13)$$

$$S_v = \frac{\partial}{\partial x}\left(\mu_t \frac{\partial u}{\partial y}\right) + \frac{\partial}{\partial y}\left(\mu_t \frac{\partial v}{\partial y}\right) + \frac{\partial}{\partial y} 4C_D C_\mu \mu_t \frac{k}{\varepsilon} \times \left[-\left(\frac{\partial v}{\partial x}\right)^2 + \frac{\partial}{\partial x}\left(u\frac{\partial v}{\partial y}\right) + \frac{\partial}{\partial y}\left(v\frac{\partial v}{\partial y}\right)\right] + \frac{\partial}{\partial x} 4C_D C_\mu \mu_t \frac{k}{\varepsilon}\left[\frac{\partial}{\partial x}\left(u\frac{1}{2}\left(\frac{\partial u}{\partial y} + \frac{\partial v}{\partial x}\right)\right) + \frac{\partial}{\partial y}\left(v\frac{1}{2}\left(\frac{\partial u}{\partial y} + \frac{\partial v}{\partial x}\right)\right) - \frac{\partial u}{\partial y}\frac{\partial v}{\partial y} - \frac{\partial u}{\partial x}\frac{\partial v}{\partial x}\right]. \quad (14)$$

The effect of t_1, t_2, and t_3 on the velocity is found to be small. The omission of t_1, t_2, and t_3 results in only a 2% change in the recirculation length and improves the solution convergence considerably. Therefore, t_1, t_2, and t_3 are neglected in the equations for the nonlinear k–ε model.

THE EXPERIMENTAL SETUP AND PROCEDURE

In the experimental setup air is drawn into the duct through a 5.25-to-1 contraction section containing a honeycomb baffle and four screens. The inlet to the test section was 40 hydraulic diameters downstream of the duct inlet. The velocity profile at this location contained a small potential core region. It was found that inside the boundary layer, the profile fit a turbulent fully developed flat plate profile, $u/u_c = (y/\delta_u)^{1/5.6}$ [21], to within 5%, where u_c is the channel centerline velocity and δ_u is the velocity boundary layer thickness. The test section (101.6 cm-long × 30 cm-wide × 6.1 cm-high) was followed by an afterduct, diffuser and a blower, operating in the suction mode. Eight 6.35 × 6.35-mm square steel ribs were evenly

distributed over the length of the lower wall of the test section.

The flow measurements were performed using a two-color DANTEC fiber-optic LDV system with a Bragg cell. The signal collected is processed using the Dantec PDA signal processor and SIZEware software.

The flow was seeded using atomized distilled water, which was introduced into the flow at the inlet to the contraction section. Each measurement consisted of 2000 samples recorded at a sampling rate that varied from 25 samples s^{-1} in the near-wall recirculating region to 1500 samples s^{-1} at the outer edge of the shear layer. Measurements for sample sizes ranging from 2000 to 10 000 samples were performed at various locations with less than a 1% difference in the mean and r.m.s. values. As recommended in ref. [22], mean velocities and Reynolds stresses were obtained by ensemble averaging without bias correction. The uncertainties were calculated to be $\pm 3.5\%$ for the mean velocities, $\pm 5\%$ for the turbulent kinetic energy, and $\pm 8\%$ for the turbulent shear stresses.

For the heat transfer experiments, a constant heat flux boundary condition was simulated by dissipating d.c. current in a 0.025-mm-thick stainless steel shim epoxied to the bottom wall of the test section. Eight balsa-wood ribs with exactly the same dimensions as the steel ribs described earlier were affixed to the upper surface of the shim at even intervals using double-sided tape. The first rib was positioned so that its upstream face was flush with the leading edge of the shim.

Chromel–constantan thermocouples (0.076 mm diameter) spot welded to the under side of the shim at 5.1-mm intervals along the centerline were used to measure the local shim temperatures. Thermocouples positioned at off-centerline locations confirmed that the spanwise temperature variation was less than 4% of the minimum shim-to-bulk fluid temperature difference. The maximum effect of the heating current on the measured thermocouple voltage was less than 12 μV (0.2°C), which is within the uncertainty of the temperature measurement.

Local Nusselt number results for the heated wall of the test section were determined from the local convective heat flux and the measured shim temperatures. The local convective heat flux was determined by subtracting conduction and radiation heat losses from the local electric heat flux generation, which was determined from measurements of the current supplied to the shim and the temperature-dependent electrical resistivity of the shim. A finite difference procedure was used to compute the conduction heat losses. The temperatures measured along the shim and along the inner surfaces of the side walls and top wall of the test section were used as boundary conditions in the heat conduction code. Both the conduction and radiation heat losses were 5% of the local electric heat flux generation. The uncertainty in the local Nusselt numbers is $\pm 5\%$. For all the experiments, $Gr_H/(Re_H)^2 < 0.002$, where Gr_H and Re_H are the duct-height based Grashof and Reynolds numbers, respectively, and Gr_H is based on the maximum shim-to-inlet temperature difference, so buoyancy effects were negligible.

From the measured Nusselt number distributions in the duct, it was observed that the distribution became periodic after the sixth rib, signalling the attainment of periodic fully developed conditions. The experimental results used in the comparisons of this study are those between the seventh and eighth ribs.

NUMERICAL ANALYSIS

The computational algorithm is based on the control volume finite difference procedure described in ref. [23]. In this procedure, the domain (see Fig. 1) is discretized by a series of control volumes, with each control volume containing a grid point. The differential equation is expressed in an integral manner over the control volume, and power-law profile approximations [23] are made in each coordinate direction, leading to a system of algebraic equations that can be solved in an iterative manner.

The periodic nature of the velocity and temperature boundary conditions require special modifications in the equation solver. The cyclic Tri-Diagonal Matrix Algorithm (cyclic TDMA) proposed in ref. [2] is used along the constant-y lines where periodic conditions apply. Along the solid boundaries, either the value of the dependent variable or the flux is specified, and the standard TDMA technique is used. It should be pointed out that the heat flux was set at zero on the surfaces of the ribs and that a constant heat flux was specified along the bottom wall between the two ribs. The handling of the periodic condition will now be described.

For a periodic fully developed flow, the pressure and temperatures are separated into two parts:

$$p(x,y) = -\beta x + p_p(x,y); \quad T = \gamma x + T_p \quad (15)$$

where $p_p(x, y)$ and T_p represent the periodic part, β is the channel pressure drop per unit length and γ, for the constant heat flux condition, is obtained from the following energy balance

$$\gamma = \frac{q''}{\rho u_{ref} H C_p}. \quad (16)$$

Rewriting the transport equation for the thermal energy (equation (7)) in terms of T_p, gives

$$\rho\left(u\frac{\partial T_p}{\partial x} + v\frac{\partial T_p}{\partial y}\right) = \frac{\partial}{\partial x}\left(\frac{\mu_t}{Pr_t}\frac{\partial T_p}{\partial x}\right) + \frac{\partial}{\partial y}\left(\frac{\mu_t}{Pr_t}\frac{\partial T_p}{\partial y}\right) - \rho\gamma u. \quad (17)$$

To achieve the desired Reynolds number, the mean channel pressure gradient (β) is corrected after each iteration using the equation given by ref. [3]:

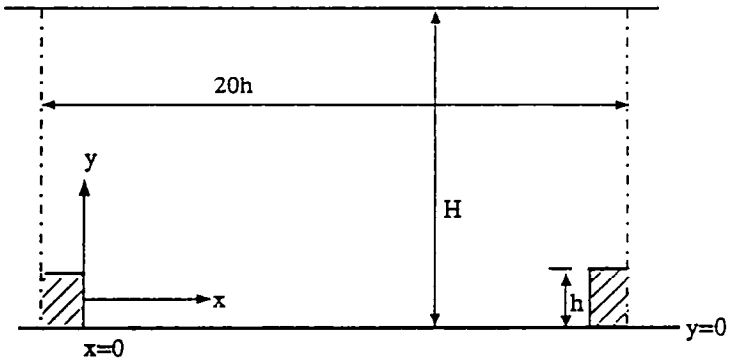

FIG. 1. Schematic of the physical situation and computational domain.

$$\beta_{new} = \beta_{old}\left(1+\alpha\left(\left(\frac{Q_0}{Q}\right)^2-1\right)\right) \tag{18}$$

where Q_0 is the desired flow rate, Q is the present calculated flow rate, and α is an over relaxation factor. A value of $\alpha = 35$ led to a satisfactory convergence rate. For Q_0/Q values that cause β_{new} to have a different sign than β_{old}, the use of equation (18) causes oscillations in β. Therefore, another correction equation for β is employed to handle this situation:

$$\beta_{new} = \beta_{old}+\alpha\left(\left(\frac{Q_0}{Q}\right)^2-1\right). \tag{19}$$

To increase the convergence rate, the β corrections are performed before correcting the velocities using the pressure correction terms.

For the nonlinear model, box-filtration [24] must be used in order to achieve convergence. The velocity fields are filtered once before calculating their gradients, and the shear stress terms are filtered three times before using them in the source and generation terms of the momentum equations.

Computations were performed using three sets of grids: 30×28, 72×38, and 120×55. Predictions of the velocity profiles at two interrib locations using the two k–ε models at the different grid settings are given in Fig. 2. It is seen that the 72×38 grid produces solutions that are virtually grid independent. The recirculation lengths predicted by the three grid sets were within 5% of each other. This study uses the 120×55 grid exclusively in order to obtain smoother Reynolds stress profiles.

RESULTS AND DISCUSSION

Table 1 shows the predictions of the reattachment length (x_R), the mean pressure gradient (β), the maximum Nusselt number (Nu_{max}) location and the maximum y^+ (y^+_{max}) location. The measured value of x_R and the measured Nu_{max} location are also tabulated. Like the wall function formulation, the calculation of y^+ is based on equilibrium considerations which lead to $y^+ \sim (k)^{1/2}$.

Table 1 shows that both models predict nearly the same reattachment length and that the predicted lengths are within the experimental error of the measured value. It is also observed that the location of the maximum Nusselt number occurs upstream of the reattachment point, with the predicted locations lying on either side of the measured value, within the experimental uncertainty. For periodically developed ribbed-duct flows, Liou and Hwang [18] determined experimentally that the maximum Nusselt number location occurs between 0.5 and 1.0 rib heights upstream of reattachment.

Turning to the location of the y^+_{max} value, it is observed that the maximum Nusselt number is found to occur between the location of the maximum y^+ value and the location of flow attachment, indicating that the point where the near-wall k value reaches its maximum is upstream of the location of the maximum Nusselt number. This is contrary to Vogel and Eaton's [25] finding that for flows past a backstep, the maximum Nusselt number location coincides with the maximum y^+ location.

Regarding the predictions of the mean pressure gradient, β, it is seen that the nonlinear model prediction is lower than that for the standard k–ε model. Reference [3] demonstrated that the standard k–ε model overpredicts the mean pressure gradient for a wide range of pitch-to-rib height ratios in a ribbed annulus. Therefore, the present predictions by the nonlinear model appear to be consistent with the observations of ref. [3].

Mean velocities

Figure 3 shows the streamwise velocity normalized by the average flow velocity (u_{ref}) in the channel. Immediately above the rib ($x/h = -0.5$, 0.0), the measurements show a sharp increase in the velocity at the near-wall location. The predictions show a more gradual increase in the velocity and underpredict the

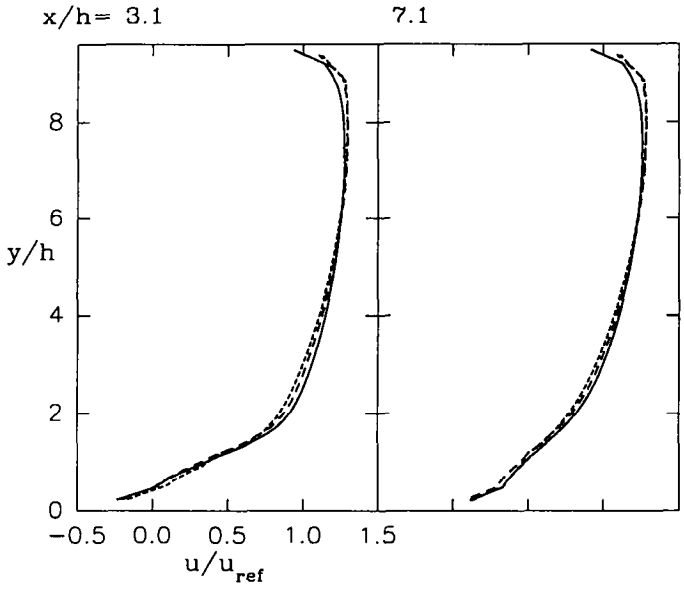

(a) Standard k–ε model.

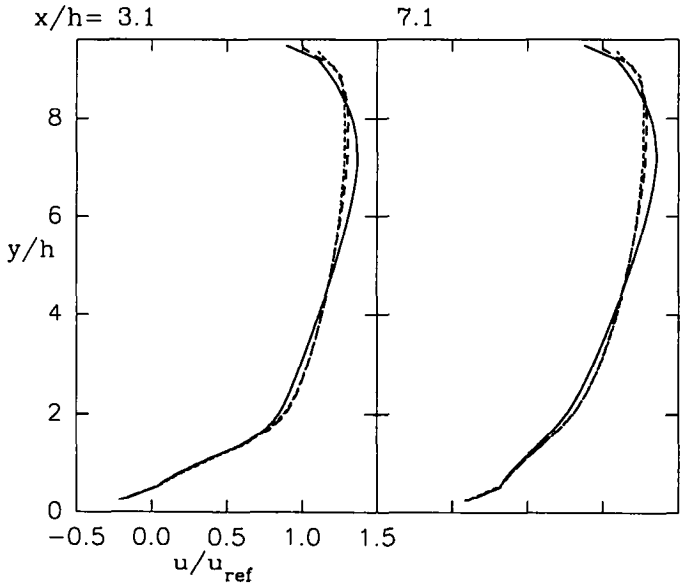

(b) Nonlinear k–ε model.

(—— 120x55 , - - - 72x38 , ----- 30x28)

FIG. 2. Effect of grid size on streamwise velocity profile.

Table 1. Predictions by standard k–ε and nonlinear models

Model	x_R/h	β	Nu_{max} location x/h	y^+_{max} location x/h
Std. k–ε	5.6	5	4.9	4.1
Nonlinear k–ε	5.7	4.83	5.4	4.4
Experimental observation	6±0.7	—	5.1±0.4	—

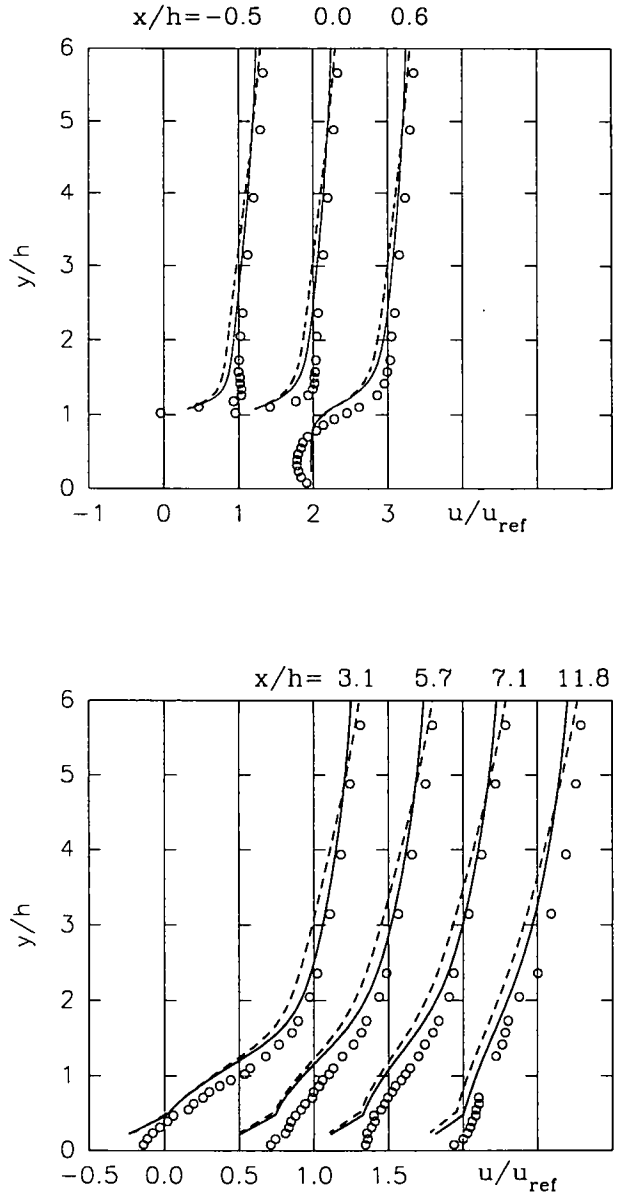

FIG. 3. Streamwise velocity distributions, $u_{ref} = 3.6$ m s^{-1}.

measured values, especially in the vicinity of the rib surface. Lower velocity gradients are predicted by the nonlinear k–ε model than by the standard k–ε model.

At the first measurement location downstream of the rib ($x/h = 0.6$), the experimental data show a stronger recirculation (larger negative velocities) than the predictions. The predicted shear layer thickness on the high velocity side at $x/h = 0.6$ is clearly greater than the measured thickness ($\delta_{u,\text{pred}}/\delta_{u,\text{meas}} = 1.43$; u at $\delta_u = 0.9\ u_{\max}$). At $x/h = 3.1$, the predicted negative velocities near the wall are higher in magnitude than the experimental observations. Beyond $x/h = 3.1$, the models underpredict the near-wall velocity, with the nonlinear model predicting lower near-wall velocities than the standard k–ε model.

The v-velocity profiles are shown in Fig. 4. Immediately above the rib ($x/h = -0.5$ and 0.0), the v velocities are positive, indicating an upward deflection of the flow by the rib. Just downstream of the rib ($x/h = 0.6$), the positive v velocities for $y/h \leqslant 1$ are due to a corner eddy. At $x/h = 3.1$ and beyond, the v velocities are negative suggesting that the shear layer is moving downward toward reattachment. Downstream of reattachment ($x/h \approx 6$), the magnitudes

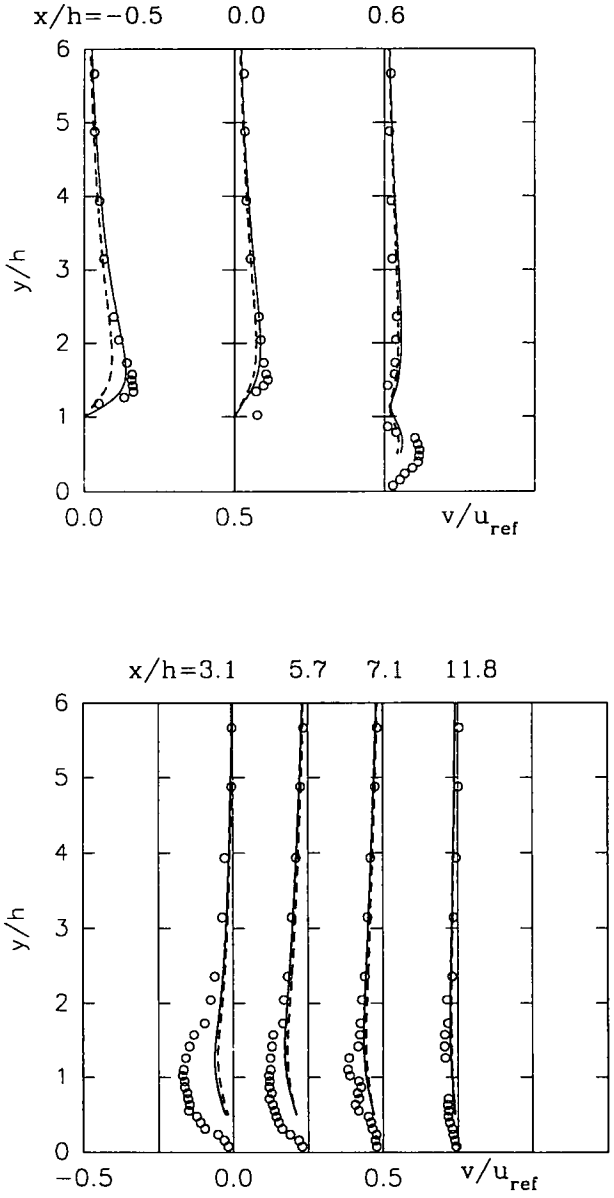

(o Experimental data,——Standard k–ε model,- - -Nonlinear model)

FIG. 4. Cross-stream velocity distributions, $u_{ref} = 3.6$ m s^{-1}.

of the v velocities decrease as the flow starts to redevelop.

The predictions by both models are found to be almost identical to each other at all locations, except $x/h = -0.5$, where the standard k–ε model performs better than the nonlinear model. It is seen that both models underpredict the velocity magnitudes in the region bounded by $0.6 \leqslant x/h \leqslant 5.7$ and $0 \leqslant y/h \leqslant 2$, which roughly corresponds to the separation bubble. Note that the corresponding u velocities were also underpredicted in this region, as required by continuity.

Turbulent stresses

Between $x/h = -0.5$ and 0.6, Fig. 5 shows that the measured $(\overline{u'^2})^{1/2}$ increases sharply in the shear-layer region close to the rib, with the peak decreasing between $x/h = 0.6$ and 3.1. Near reattachment ($x/h \approx 6$), the measured profile is flatter than at $x/h = 3.1$, and the peak fluctuations have diminished. With further increases in x/h, the experimental $(\overline{u'^2})^{1/2}$ profile continues to flatten out, and the fluctuations continue to decay, indicative of the strong damping effect induced by the wall. Also noteworthy is the fact that the measured turbulence levels in the corner eddy

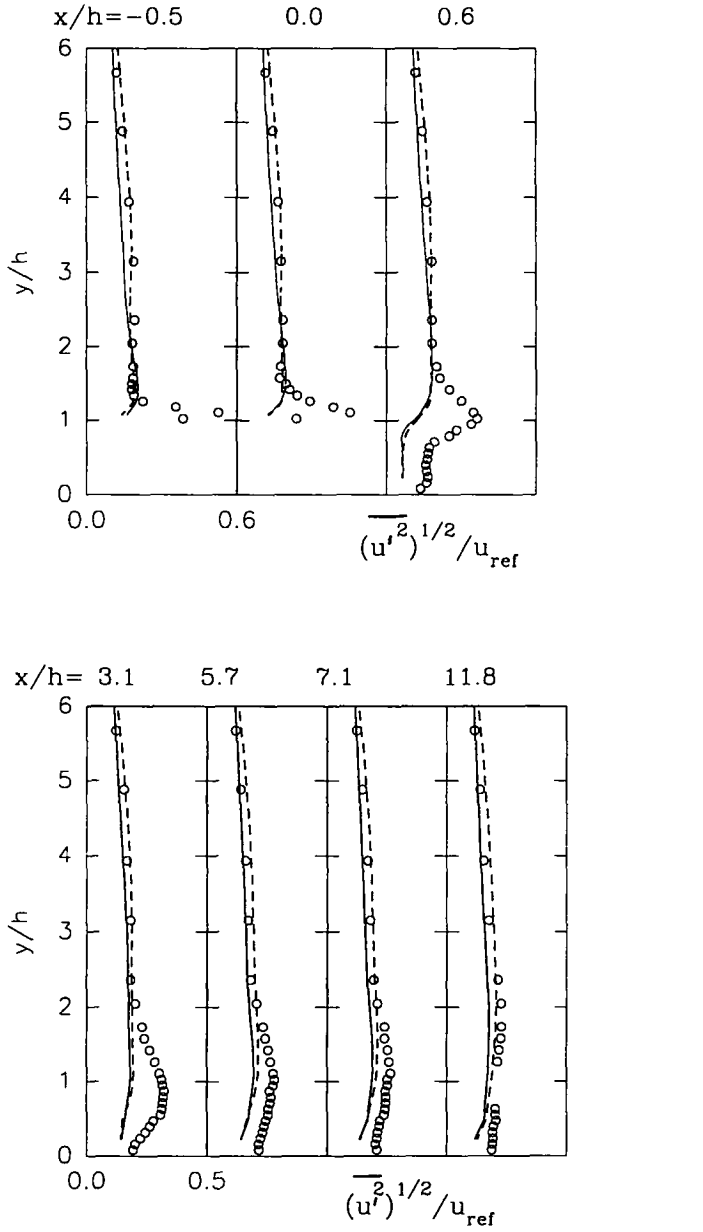

(o Experimental data,——Standard k–ϵ model,- - -Nonlinear model)

FIG. 5. Streamwise velocity fluctuations, $u_{ref} = 3.6$ m s^{-1}.

region are roughly the same as those at the duct centerline, indicating that although the velocities are low in the separated region, this region is not a low-turbulence region.

In the shear layer region between $x/h = -0.5$ and 0.6 as well as in the shear layer and recirculation regions up to $x/h = 5.7$, both models predict close to the same $(\overline{u'^2})^{1/2}$ values, with these values grossly underpredicting the measured values. However, the nonlinear model shows slightly better agreement with the measured values in the core-flow region immediately above the rib ($x/h = -0.5$ and 0.0). The agreement between the predictions of both models and the measured results is comparable and quite satisfactory in the core-flow region downstream of the rib, where the velocity gradients are insignificant.

Compared to backstep flows, the profiles are more uniform. This is because the upward deflection of the flow by the ribs induces larger velocity gradients above the rib, leading to higher turbulence levels in the above-rib regions. Thus, the nonuniformity in the turbulence profiles is reduced.

Figure 6 shows that the measured $(\overline{v'^2})^{1/2}$ distributions follow a streamwise evolution downstream of the rib that is similar to the measured $(\overline{u'^2})^{1/2}$ distributions. It is also observed that the nonlinear model

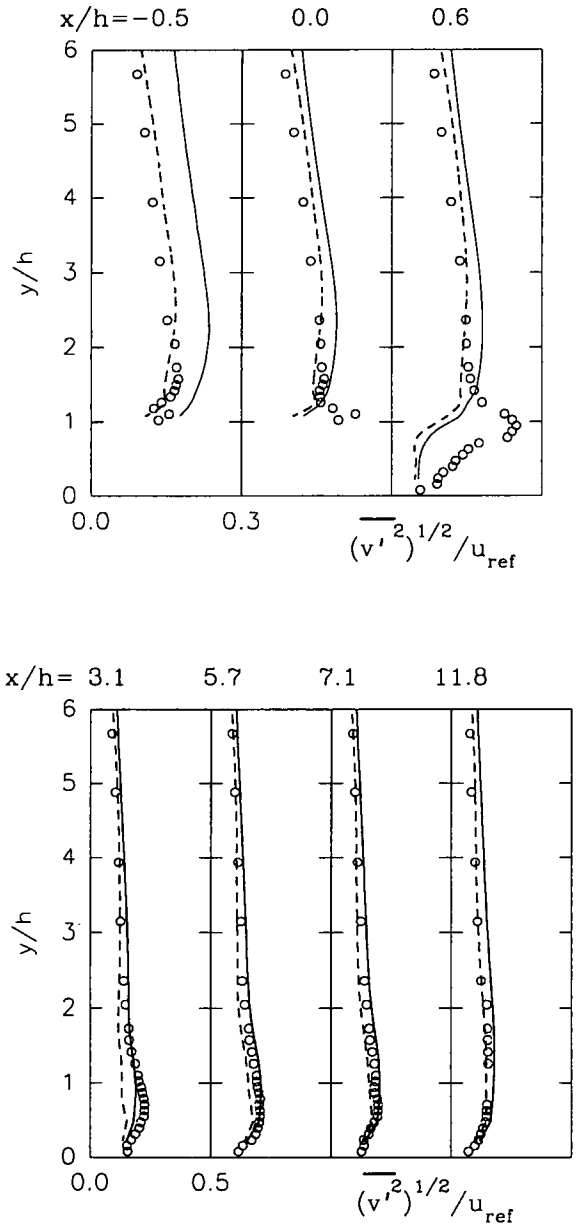

(o Experimental data,——Standard k–ε model,- - -Nonlinear model)

FIG. 6. Cross-stream velocity fluctuations, $u_{ref} = 3.6$ m s^{-1}.

predicts $(\overline{v'^2})^{1/2}$ quite well in the core-flow region between $x/h = -0.5$ and 0.6, while the standard k–ε model overpredicts the measured values. In fact, at $x/h = -0.5$ and 0.0, contrary to the measurements, the standard k–ε model predicts $(\overline{v'^2})^{1/2}$ values that are higher than the $(\overline{u'^2})^{1/2}$ values. In the separated region, at $x/h = 0.6$, both models underpredict the measurements and fail to predict a peak at $y/h = 1.0$, as they did for the $(\overline{u'^2})^{1/2}$ distribution. Further downstream, both models perform rather well in both the near-wall and core-flow regions, with the standard k–ε model performing slightly better close to the wall at $x/h = 3.1$ and 5.7.

An examination of the turbulent shear stress $(\overline{u'v'})$ distributions in Fig. 7 reveals a dramatic increase in $\overline{u'v'}$ just after the rib ($x/h = 0.6$). At 3.1 rib heights downstream of the rib, the turbulent shear stress distribution is broader, and the peak value has diminished considerably. This trend continues with further increases in x/h.

It is clear from Fig. 7 that both models grossly underpredict the turbulent shear stress behind the rib

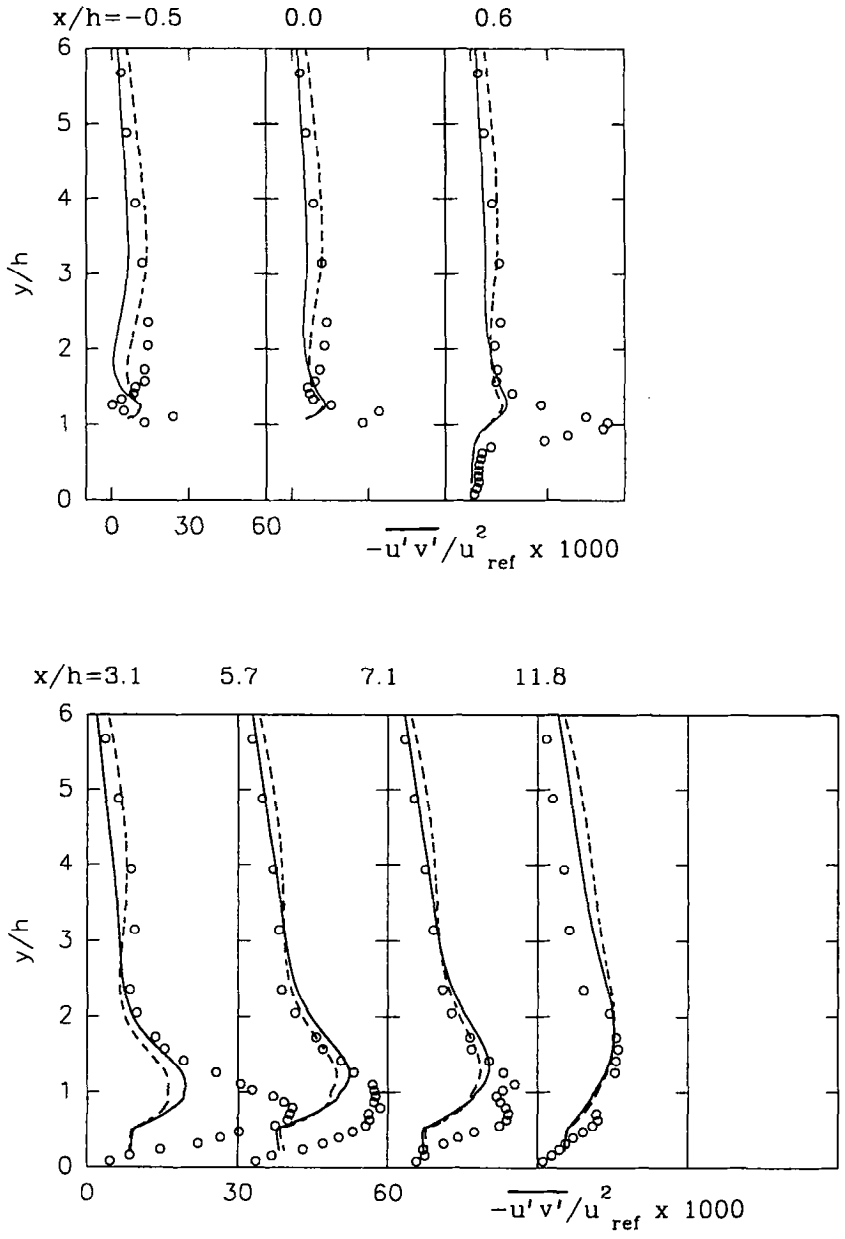

(o Experimental data,——Standard k–ε model,- - -Nonlinear model)

FIG. 7. Turbulent shear stress distributions.

up to reattachment ($x/h \approx 6$), with the standard k–ε model performing slightly better than the nonlinear model. It is speculated that the large-scale effects are creating the discrepancies between the measurements and the predictions, which are based on the modeling of the small-scale turbulence. In this respect, both models, perform better in the core flow region at all x/h locations.

Heat transfer and temperature results

Figure 8 shows the predicted and experimental Nusselt number results. The local Nusselt number is determined from $Nu = q''D/(K(T_w(x) - T_b(x)))$, where D is the hydraulic diameter of the duct ($D = 101.6$ mm) and K is the thermal conductivity based on $(T_w(x) + T_b(x))/2$. The measured Nusselt number reaches a maximum at $x/h = 5.1$. This corresponds to a location just upstream of the measured reattachment location. It was pointed out earlier that the predicted Nu_{max} locations were both within the experimental uncertainty of the measured value. The Nusselt number is underpredicted by both models. Though the nonlinear model shows improvement in $(\overline{u'^2})^{1/2}$ and $(\overline{v'^2})^{1/2}$, no such improvement can

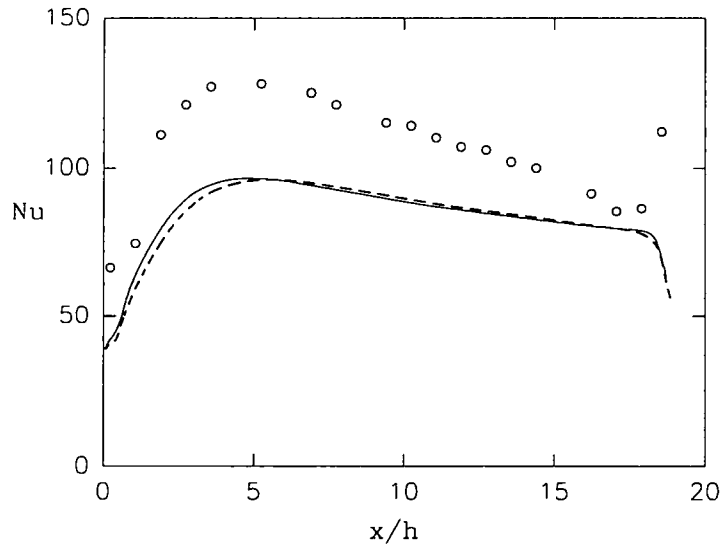

FIG. 8. Local Nusselt number distributions.

be seen in the magnitude of the predicted Nusselt number.

The measurements show a peak just upstream of the eighth rib, resulting from a separation of the flow as it encounters the downstream rib. Sparrow and Tao [1] also observed a peak in the local heat transfer coefficient just upstream of each rib and attributed this peak to the presence of an intense, compact vortex in this region. Both models also predict a small separation near the downstream rib but do not reflect a detectable peak in the predicted local Nusselt number profile.

Nondimensional temperature profiles for different locations downstream of the rib are displayed in Fig. 9. Similar to the behavior discussed in conjunction with the flow results, both models perform rather poorly immediately behind the rib. It is speculated that a use of a constant value for Pr_t in predicting the temperatures in the strong mixing region of the shear layer contributes to the disparity between the predicted and measured results. The figure also shows that the agreement between both models and the measurements improves considerably in the core-flow region above the rib for all x/h values and for all y/h values at $x/h = 4.7$ and 17.4. Note that the profiles predicted by both models are virtually identical at all locations, thus explaining the virtually identical Nusselt number plots.

The underprediction of the Nusselt number at $x/h = 4.7$, in spite of the good agreement between

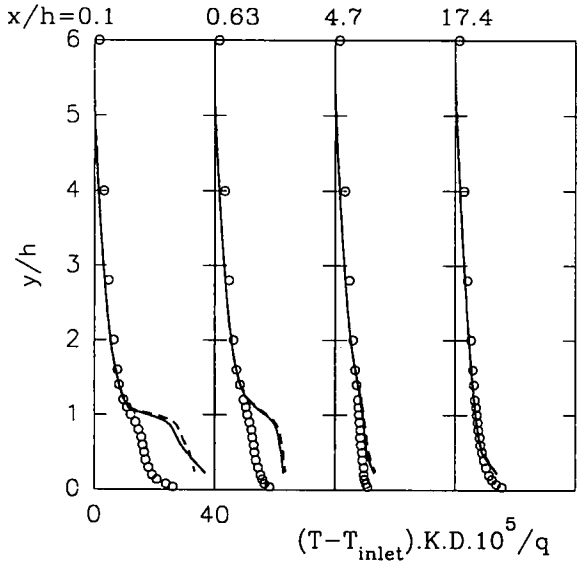

FIG. 9. Mean temperature distributions.

the predicted and measured temperature profiles, is related to the inadequacies of the wall functions in the separated region. Although improved wall functions will result in better Nusselt number predictions, they will not necessarily lead to improvements in the predicted temperature profiles immediately behind the rib. This is because for the constant heat flux condition, the numerical procedure calculates the fluid temperature first with the specified heat flux at the boundary; then, the wall temperature is computed using wall functions and the constant heat flux condition. Therefore, the wall temperature depends on the choice of the wall function for the temperature and the predicted temperature profiles in Fig. 9 are not directly dependent on the wall function (indirect effects come from the velocity predictions).

CONCLUDING REMARKS

The ability of the nonlinear k–ε turbulence model to predict the flow and heat transfer between successive two-dimensional ribs in the periodic fully developed regime of a rectangular duct with ribs periodically distributed along the length of the uniformly heated bottom wall was assessed through comparisons with the standard k–ε turbulence model and experimental measurements. It was found that the nonlinear model predicted more realistic Reynolds stresses than the standard k–ε model in the region immediately above the ribs. Both models generally predicted the measured Reynolds stresses quite well in the core-flow region up to reattachment and at all flow locations downstream of reattachment. However, in the recirculation and shear layer regions immediately behind the ribs, both models grossly underpredicted the Reynolds stresses. It is believed that this is because both models do not directly account for the large-scale effects which are present in this region.

Both models predicted essentially the same mean velocity profiles. In the recirculation and shear layer regions just behind the ribs, both models performed poorly. However, adequate predictions were obtained for the rest of the flow field.

Virtually the same reattachment lengths were predicted by both models and were in good agreement with the measured values. The predicted maximum Nusselt number locations occurred on either side of the measured location, within the measurement uncertainty. However, both models underpredicted the local Nusselt numbers. This was attributed to inadequacies in the wall functions.

Comparisons of the computed and measured flow temperatures revealed that both models performed poorly in the recirculation region just behind the ribs. This was attributed to the use of a constant turbulent Prandtl number in this region of strong mixing. In the core-flow region and in the interrib regions sufficiently downstream of the ribs, both models predicted the flow temperature quite well.

Acknowledgements—This work was supported by funds from the National Science Foundation and the Cornell National Supercomputing Facility. Their support is gratefully acknowledged.

REFERENCES

1. E. M. Sparrow and W. Q. Tao, Enhanced heat transfer in a flat rectangular duct with streamwise periodic disturbances at one principal wall, *J. Heat Transfer* **105,** 851–861 (1983).
2. S. V. Patankar, C. H. Liu and E. M. Sparrow, Fully developed flow and heat transfer in ducts having streamwise-periodic variations of cross-sectional area, *J. Heat Transfer* **99,** 180–186 (1977).
3. B. K. Lee, N. H. Cho and Y. D. Choi, Analysis of periodically fully developed turbulent flow and heat transfer by k–ε equation model in artificially roughened annulus, *Int. J. Heat Mass Transfer* **31,** 1797–1806 (1988).
4. M. A. Leschziner and W. Rodi, Calculation of annular and twin parallel jets using various discretization schemes and turbulence model variations, *J. Fluid Engng* **103,** 352–360 (1981).
5. C. G. Speziale, On nonlinear k–l and k–ε models of turbulence, *J. Fluid Mech.* **178,** 459–475 (1987).
6. B. E. Launder and D. B. Spalding, The numerical computation of turbulent flows, *Computer Methods in Applied Mechanics and Engineering* **3,** 269–289 (1974).
7. S. Thangam and C. G. Speziale, Turbulent separated flow past a backward-facing step: A critical evaluation of two-equation turbulent models, *ICASE Report No.* 91-23 (1991).
8. C. G. Speziale and T. Ngo, Numerical solution of turbulent flow past a backward facing step using a nonlinear k–ε model, *Int. J. Engng Sci.* **26**(10), 1099–1112 (1988).
9. S. Thangam and N. Hur, A highly-resolved numerical study of turbulent separated flow past a backward-facing step, *Int. J. Engng Sci.* **29**(5), 607–615 (1991).
10. S. Dutta, A numerical study of turbulent flow and heat transfer in a ribbed duct with two equation turbulence models, M.S. Thesis, Louisiana State University, Baton Rouge, Louisiana (1992).
11. F. Durst and A. K. Rastogi, Turbulent flow over two-dimensional fences. In *Turbulent Shear Flows 2* (Edited by Bradbury *et al.*), pp. 218–231. Springer-Verlag, Berlin (1980).
12. R. W. Benodekar, A. J. H. Goddard, A. D. Gosman and R. I. Issa, Numerical prediction of turbulent flow over surface-mounted ribs, *AIAA J.* **23**(3), 359–366 (1985).
13. M. K. Chung, S. W. Park and K. C. Kim, Curvature effect on third-order velocity correlations and its model representation, *Physics Fluids* **30**(3), 626–628 (1987).
14. S. W. Park and M. K. Chung, Curvature-dependent two-equation model for prediction of turbulent recirculating flows, *AIAA J.* **27,** 340–344 (1989).
15. F. Durst, M. Founti and S. Obi, Experimental and computational investigation of the two-dimensional channel flow over two fences in tandem, *J. Fluid Engng* **110,** 48–54 (1988).
16. T. M. Liou, Y. Chang and D. W. Hwang, Experimental and computational study of turbulent flows in a channel with two pairs of turbulence promoters in tandem, *J. Fluid Engng* **112,** 302–310 (1990).
17. J. F. Lockett and M. W. Collins, Holographic interferometry applied to rib-roughness heat transfer in turbulent flow, *Int. J. Heat Mass Transfer* **33,** 2439–2449 (1990).
18. T. M. Liou and J. J. Hwang, Turbulent heat transfer augmentation and friction in periodic fully developed channel flows, *J. Heat Transfer* **114,** 56–64 (1992).
19. J. C. Han, P. R. Chandra and S. C. Lau, Local heat/mass transfer distributions around sharp 180° turns in two-

pass smooth and rib-roughened channels, *J. Heat Transfer* **110**, 91–98 (1988).
20. J. C. Han, Heat transfer and friction characteristics in rectangular channels with rib turbulators, *J. Heat Transfer* **110**, 321–328 (1988).
21. D. E. Abbott and S. J. Kline, Experimental investigation of subsonic turbulent flow over single and double backward facing steps, *J. Basic Engng* **84**, 317–325 (1962).
22. D. M. Driver and H. L. Seegmiller, Features of a reattaching shear layer subject to adverse pressure gradient, *AIAA-82-1029, AIAA/ASME 3rd Joint Thermophysics, Fluids and Heat Transfer Conference*, June, St. Louis, MO (1982).
23. S. V. Patankar, *Numerical Heat Transfer and Fluid Flow*. Hemisphere, Washington, D.C. (1980).
24. R. A. Clark, J. H. Ferziger and W. C. Reynolds, Evaluation of subgrid-scale models using an accurately simulated turbulent flow, *J. Fluid Mech.* **91**(1), 1–16 (1979).
25. J. C. Vogel and J. K. Eaton, Combined heat transfer and fluid dynamic measurements downstream of a backward-facing step, *J. Heat Transfer* **107**, 922–929 (1985).